Platinum Stability

2010 Progress Report

Thomas F. Fuller, Professor and Director
Center for Innovative Fuel Cell and Battery Technologies
School of Chemical & Biomolecular Engineering

Georgia Institute of Technology
Atlanta GA 30332

Graduate Research Assistant:
Erin L. Redmond

Postdoctoral Fellow
Panos Trogadas

September 30, 2010

Pair Distribution Function

Introduction

Proton exchange membrane fuel cells (PEMFCs) are competitive with other emerging technologies being considered for automotive transportation. Commercialization of PEMFCs would decrease emissions of criteria pollutants and greenhouse gases and reduce US dependence on foreign oil. However, many challenges exist that prevent this technology from being realized, including power requirements, durability, on-board fuel storage, fuel distribution, and cost. This project will focus on fuel cell durability, or more specifically catalyst stability.

PEMFC degradation can be categorized into three topics: membrane degradation, carbon corrosion, and catalyst stability. The membrane in PEMFCs is designed to conduct protons and to separate the fuel from the oxidant.[1] Nafion® is typically used since it possesses a relatively high chemical stability in fuel cell applications[2] and it is able to maintain high proton conductivity over a wide range of relative humidity conditions.[3] Optimizing the performance of Nafion® requires fully humidified reactant streams and the use of thinner membranes to lower proton transfer resistance. Adversely, thinner membranes are more susceptible to degradation and increase gas permeability.[1] Chemical degradation occurs when crossover H_2 and O_2 react to form H_2O_2, which then reacts with metal impurities of the catalyst forming harmful peroxide radicals *OH and *OOH. These radicals then attack the weak polymer chain resulting in membrane degradation, which has been identified as the primary degradation mechanism in Nafion®. [1, 2] Research continues in membrane degradation focusing on mitigation techniques that aim to reduce trace metal contaminants, optimize relative humidity conditions and membrane thickness to decrease gas permeability, and minimize radical formation through the use of free radical scavengers, such as ceria.[1, 4]

Carbon is used as a catalyst-support due to its high surface area, electrical conductivity, low cost, and abundant supply. Carbon blacks, such as Vulcan XC-72, are typical catalyst-supports used in PEMFC applications.[5, 6] Major contributors to carbon instability are oxidants and the high potentials reached during start-up/shut-down or idle conditions of the fuel cell. [5] The proposed path of degradation is described by the reverse-current mechanism in which crossover oxygen is reduced at the anode and, in the absence of hydrogen, protons are supplied from the cathode by either carbon oxidation or oxygen evolution from water.[5, 6] Fuel starvation occurs due to blocked gas-flow channels. The electrode is significantly damaged after 5 to 10 percent carbon weight loss occurs.[6] Graphitization of carbon reduces the weight loss percentage seen in fuel cells, but also reduces the surface area, which limits catalyst dispersion.[5] Enhancing the oxygen evolution reaction by incorporating a selective catalyst on the carbon support is another approach to mitigate carbon oxidation. The reverse current is generated by the oxygen evolution reaction at less positive potentials in place of carbon oxidation.[6] The economic viability of carbon will ensure continued progress in carbon corrosion mitigation research for use in fuel cell systems.

Platinum has a relatively high kinetic activity for the oxygen reduction reaction (ORR) and is resistant to corrosion, both of which are desirable properties for a fuel cell catalyst. However, platinum is unstable during certain points of fuel cell operation resulting in catalyst loss. At high potentials, above 0.8 V vs reference hydrogen electrode (RHE), an oxide layer forms on the platinum surface, and as the layer becomes unstable, platinum and oxygen undergo a place

exchange.[7] Upon reduction, platinum ions are formed, which have a finite solubility at high potentials and low pH as shown in the platinum Pourbaix diagram below.[8]

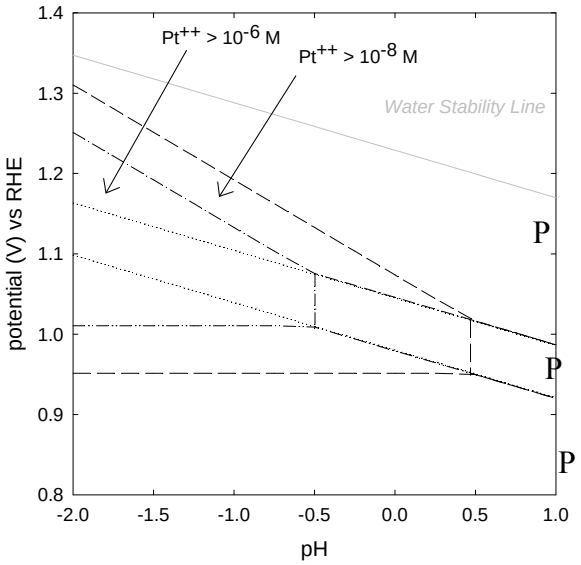

Figure 1 Pourbaix diagram[8] for platinum at room temperature shown for upper potential limits of fuel cell operation. Also shown is the curve shift associated with varying Pt^{2+} concentrations.

Both conditions exist in PEMFCs since high potentials are reached during start-up, shut-down, and idle periods of fuel cell operation, and the electrolyte, typically Nafion®, is highly acidic. Consequently, platinum dissolves into the electrolyte. Platinum can either recrystallize on larger particles, contributing to Ostwald ripening or diffuse into the membrane and precipitate, forming a platinum band. Both mechanisms contribute to reducing the electrochemically active area of the catalyst layer; thereby, reducing fuel cell efficiency.[9] Additionally, the platinum band can generate high stress areas inside the membrane making it more susceptible to degradation.[1]

Platinum nanoparticles are used to decrease the overall platinum loading on the electrode, while maintaining the necessary catalytic surface area to drive the reactions.[10, 11] However, there is a lower limit on particle size as particles smaller than 5 nm have been shown to be unstable and coarsen via Ostwald ripening.[10, 12] In addition to losing active catalyst area and reducing fuel cell efficiency, this process necessitates the use of higher than desired platinum loadings corresponding to an increased manufacturing cost.

During the past year, the project focus has been on enhancing the fundamental understanding of catalyst stability in PEMFCs. The pair distribution function (PDF) method has been applied to an ex-situ study of various sized platinum particles supported on carbon. The PDF is a physics-based technique that has been successfully implemented to study the local structure of non-periodic systems.[13] Utilizing the PDF technique will provide insight to changes in atomic distances due to surface energy deviations from bulk particles, which affects platinum stability. Additionally, the PDF provides a method to monitor platinum movement throughout the lifetime of a fuel cell. The following sections will provide necessary background information that will be used to support motivation for future work. The focus will be information about PDF and results obtained from preliminary experiments.

Literature review

Platinum dissolution studies

Throughout the lifetime of a fuel cell the cathode loses a significant amount of electrochemically active surface area (ECA). Platinum dissolution was first observed in phosphoric acid fuel cells in the 1970s,[14-17] and the mechanism governing platinum deterioration is similar to that found in PEMFCs. Shao-Horn and coworkers classified four mechanisms responsible for ECA loss: (i) Ostwald ripening, (ii) coalescence, (iii) particle detachment from the carbon support, and (iv) platinum diffusion into the electrolyte.[18] The first mechanism is large particle growth at the expense of small particles via an Ostwald ripening type process (Figure 2a).[16-18] Due to the effects of surface energy and particle curvature, small particles have a higher solubility than large particles. As a result, upon oxidation of platinum, ions diffuse through the electrolyte from small to large particles, where reduction and redeposition occur. Secondly, coalescence may occur due to crystal migration (Figure 2b) where particles randomly collide and stick together.[18]

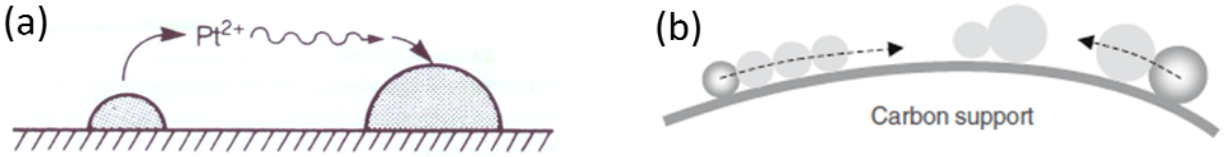

Figure 2 (a) Ostwald ripening mechanism[17] and (b) coalescence by particle migration[18].

Both mechanisms are driven by a reduction in surface energy and can be distinguished by particle size distribution (PSD) analysis.[18] Ostwald ripening will exhibit a tail at smaller particles. Conversely, coalescence will have a distinctive tail at large ends.[19, 20] Another distinguishing factor between the two mechanisms is that particle coalescence is independent of voltage, yet Ostwald ripening is driven by the upper potential limit.[19] Coalescence may be accelerated by carbon corrosion. Detachment from the carbon support and dissolution of platinum and diffusion into the membrane are proposed as further mechanisms for platinum loss.[18] This mechanism is supported by scanning electron microscopy (SEM) images showing a platinum band in the membrane seen for H_2/air cycles.[9, 19] In-situ techniques would be beneficial to enable study of particle behavior during cycling conditions.

Darling and Meyers were the first to simulate platinum dissolution in PEMFCs.[21, 22] Platinum dissolution, assumed to be a single elementary step, electrochemical formation of platinum oxide, and chemical dissolution of platinum oxide were all considered. The shift in electrochemical potential (ΔU) was modeled using the Kelvin equation (below), assuming a constant surface tension for all size regimes.[21]

$$\left|\Delta U\right| = \frac{\sigma_{Pt_{[111]}} M_{Pt}}{\rho_{Pt} r} \cdot \frac{1}{nF} \qquad (0.1)$$

In their model they used the surface tension ($\sigma_{Pt[111]}$) that corresponded to the platinum (111) surface, which has the lowest surface energy of all surface planes.[11, 21] The molecular weight (M_{Pt}), the density of platinum (ρ_{Pt}), and Faraday's constant (F) are all equal to their standard reference values. The number of electrons (n) involved in the platinum dissolution reaction is 2, associated with the Pt^{2+} oxidation state. Kinetic and thermodynamic parameters were fit to data obtained by Bindra et al. and Kinoshita et al.[15, 21, 23] Overall, a good fit was achieved, but

some deviations were observed as shape changes in the CV curve; for example, the onset of oxide reduction was predicted to begin at a more positive potential.[21] In 2005, Darling and Meyers expanded the model and allowed platinum to travel from the cathode to anode, but did not allow deposition in the membrane. A bimodal particle size distribution was incorporated to study the particle size effect. Variations between model and experimental studies were predicted to be due to the simplification of the Kelvin equation, consequences of which will be elaborated on in the next section.[22]

An extensive study was conducted by Ferreira and coworkers to investigate both nanometer (Ostwald ripening, migration) and micron (platinum band) scale mechanisms.[19] Wet cell experiments were conducted to measure platinum ion concentration as a function of potential, where a proportional relationship was found. However, the potential dependence observed was approximately ½ times weaker than predicted Nernstian behavior. This effect could be attributed to simultaneous chemical and electrochemical processes, surface morphologies, and particle size effects.[18] Short stack experiments were performed, followed by post-mortem investigations of SEM, x-ray diffraction (XRD), and transmission electron microscopy (TEM).[19] Larger particles were observed on the cathode after cycling, supporting the Ostwald ripening hypothesis.[18, 19] Additionally, non-spherical platinum agglomerates separated from the carbon support were detected close to the cathode/membrane interface. It was determined that nanometer scale dissolution and the micron scale mechanism each account for a loss of ⅓ of the total ECA.[19] The experimental observations obtained by Ferreira support the theory that dissolution is limited to the under-coordinated surface atoms, which would contribute to extreme surface distortion in nanoparticles.[18]

Bi and coworkers extended Darling and Meyers study to incorporate platinum band formation in the membrane.[24] The cathode-membrane interface was not examined. Platinum was only found in the Nafion®111 membrane after H_2/air cycles at 65 °C and 100% relative humidity. Electrochemically active area losses for H_2/air cycles were 10% less than H_2/N_2 cycles.[9] This effect was attributed to surface oxide coverage under air conditions, which stabilized platinum at high potentials. The location of the band was predicted as a function of gas permeation rates.[9] Further treatment of the model involved dissolution and redeposition at the cathode, ion transport into matrix, and ion reduction by the H_2 front present in the membrane.[24] The results support the existence of a potential transition regime where platinum ions are soluble, and cycling accelerates PEMFC degradation.[22] The upper potential limit, affects platinum stability the most, accounting for 60% of variability observed in dissolution metrics.[25] To better describe platinum dissolution accurate parameters are needed for physics-based models.

Particle-size effect

In current PEMFC catalyst degradation models the Kelvin or Gibbs-Thomson relations are used to estimate platinum stability as a function of particle size. [10, 18, 21, 22] As seen in Figure 3 and reported experimentally, steep energy changes are observed for particle diameters below 5 nm.[10, 26, 27]

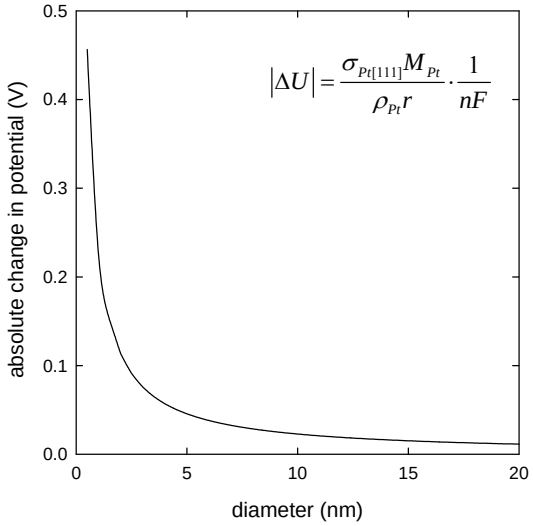

Figure 3 The change in potential versus particle diameter as predicted by the Kelvin equation (inset) where $\sigma_{Pt[111]}$ is the surface tension of the platinum (111) plane (0.237 mJ/cm^2), M_{Pt} the molecular weight of platinum (195.08 g/mol), ρ_{Pt} the density of platinum metal (21 g/cm^3), r is the particle radius, n the number of electrons transferred in platinum dissolution (2 eq/mol), and F is Faraday's Constant (96,485 C/eq).[21]

The glaring difference between a bulk sample and smaller particles is the increased percentage of surface atoms, which creates an increased surface energy affecting the physical properties of materials.[27-29] Increased percentage of uncoordinated atoms increases the surface energy of small particles, creating instability and accelerating platinum dissolution.[19] Furthermore, different crystallite faces exhibit different kinetics and surface energies, and what is observed experimentally is the average of all contributions. Spherical particles possess the lowest possible surface energy for materials; however, platinum has been shown to have non-spherical shapes in post-mortem PEMFC experiments, which would correspond to an increased surface energy.[19] Density functional theory calculations indicate that platinum supported on carbon would take the form of a truncated cuboctahedral shape.[30] Darling and Meyers' simulation of ECA loss versus time resulted in a slight downward curve because the surface tension combinations used for platinum and platinum oxide resulted in an inverse relationship between dissolution rate and particle size. The curve was not consistent with experimental data, suggesting that the surface tension values used for platinum and platinum oxide do not fully describe the system.[22] To investigate this claim it is appropriate to consider how molecular mechanics and the forces between individual molecules play a role in thermodynamics.[31]

Molecular mechanics demonstrates why smaller particles exhibit increased surface energy. Surface energy is stored as strain energy between surface atoms and those directly beneath the surface, and it is roughly proportional to the percentage of surface atoms.[28, 29] For a particle to exist, repulsive forces between atoms must be in equilibrium with attractive forces between atoms.[28] Before contraction, the total attractive force in a particle is greater than the total repulsive force; thus, the atoms must move closer together to increase the total repulsive force. This contraction results in an increased bond strain within the particle.[28] Increased lattice contractions can cause a change in the physical properties of a material.[32] For example, semiconductors of various sizes exhibit different fluorescent and luminescent properties resulting from the size dependence of energy absorption.[33, 34]

Applying molecular mechanics, Huang and coworkers developed a continuous, elastic model for predicting bond strain in metal nanoparticles[26] by extending the work of Vermaak, Mays, and Wilsdorf.[35] The study assumed spherical, metal nanoparticles, and size effects were characterized by Tolman's formula.[26, 31] Surface energy was introduced as a boundary condition where the Young-Laplace equation was assumed to characterize the stress at the surface of the particle.[26] Whereas the model results were adequate for data presented on palladium nanoparticles, the basis of the simulation was intended for a vapor-liquid system so the model may not represent an accurate pool of data. The application of this model will be discussed in the **Experimental** section.

Pair distribution function (PDF)

The PDF is a bond length distribution that reveals the average local atomic structure, in comparison to standard crystallographic techniques such as SEM, TEM, and XRD that give information regarding the average bulk structure.[36] Additionally, use of the PDF does not require the assumption of crystal periodicity, which is a key requirement for crystallographic methods.[12] The PDF, G(r), is obtained by the Fourier sine transform of the total scattering pattern, S(Q), recorded from powder diffraction data; the mathematical representation is shown below.

$$G(r) = 4\pi r[\rho(r) - \rho_0] = \frac{2}{\pi}\int_0^\infty Q[S(Q) - 1]\sin(Qr)dQ \quad (0.2)$$

The microscopic pair density and average number density are respectively represented by $\rho(r)$ and ρ_0. The magnitude of the scatter vector is labeled Q.[36] The benefit of viewing the data in real space is that it can accurately identify nearest neighbor distances; thereby revealing bond strain between atoms, chemical species present, and particle sizes.[13]

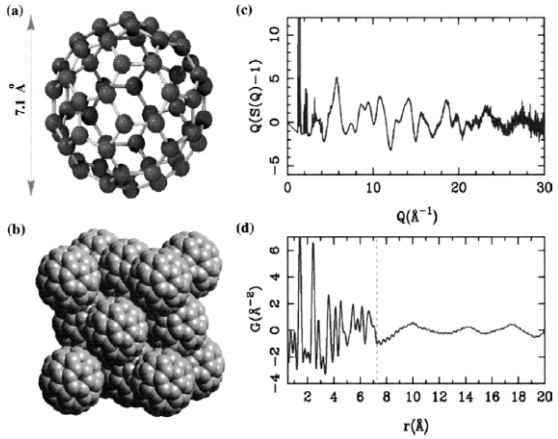

Figure 4 Local atomic structure revealed in PDF.[37]

Figure 4(a) shows a carbon-60 molecule, and the face centered cubic (FCC) structure is shown in (b). Part (c) is the total scattering pattern obtained from neutron diffraction, and (d) is the PDF representation of the data.[37] The sharp peaks reveal intramolecular (atom-atom) correlations, while the broad peaks reveal intermolecular structure (ball-ball). Only broad peaks exist after 7.1 Å (the diameter of the ball) because the atom-atom interactions cannot exceed the diameter of the particle.[37] To obtain accurate PDF data high energy sources are required,

which is a reason the PDF technique is not a dominant structure analysis tool. Generally, the measurements are carried out at synchrotron x-ray sources or pulsed neutron sources. [13]

Nanoparticles lack long range order (periodicity), which make them perfect candidates for PDF studies.[13, 37] Among many examples in which the PDF has been employed to verify crystal structure is molybdenum disulfide, MoS_2, used in petroleum refineries to remove sulfur from crude oil streams.[13, 38] Pristine MoS_2 is crystalline, but lithium is intercalated between MoS_2 layers to provide stability for future manufacturing processes that MoS_2 undergoes. Insertion of lithium causes the material to become poorly diffracting; transforming it to an unsuitable candidate for traditional crystallographic techniques which require sharp Bragg peaks for analysis. After two decades of study the structure of $LiMoS_2$ was undetermined. Finally, in 2002 Petkov and coworkers used the PDF technique to characterize the nature of the catalyst. PDF data was fit to several structural models, and the best agreement came from the assumed structure of "zigzag metal-metal" chains (Figure 5).[38]

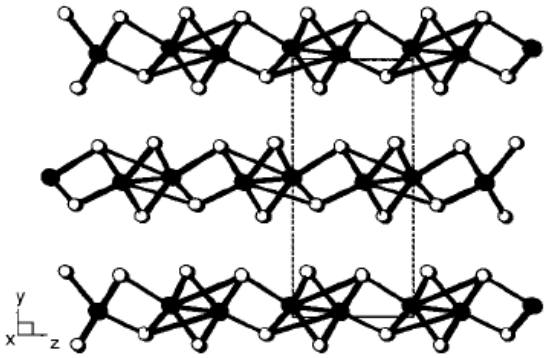

Figure 5 Representative example of zigzag metal-metal chains for WS_2 structure from Petkov et al. (2000).[39] The same structure was assumed for $LiMosS_2$.[38]

Experimental

Preliminary data has been collected in an effort to apply PDF analysis to determine the surface energy as a function of particle size for platinum nanoparticles. The PDF technique requires the use of a high energy beam line. Samples were prepared and tested at Argonne National Lab, beam line 11-ID-B. In collaboration with Professor Simon Billinge's group (Columbia University), samples were tested to identify nearest neighbor distances to determine the correlation between bond distance and particle size. Temperature scans were also completed. The following sections will provide information on the materials used, instruments and analytical methods applied, and experimental results. The section will follow with proposed future experiments. In preliminary studies bond strain as a function of particle size has been determined.

Materials and characterization

In preliminary studies, four carbon-supported platinum catalyst samples of varying weight percentages were obtained from Tanaka Kikinzoku Group (TKK). Samples of platinum loaded on carbon in various weight percentages were characterized using XRD, TEM, CO adsorption, and N_2 BET adsorption by TKK. Tanaka sent one TEM image per sample and directly reported metal surface area, catalyst surface area, and diameter determined from XRD data. Equipment

specifications and experimental operating conditions were not identified. Particle diameters were measured with a ruler from the TEM images and the data were normalized by the total number of particles counted. The samples were represented by wide particle size distributions (PSDs). This observation is significant as it accounts for some experimental error, and may be a foreseeable issue. The PDF reveals the average local structure; therefore, if particles of different sizes contribute to the average, error will be seen in the data. Samples with very small (0.5 to 1.5 nm) average particle diameters were not considered in this study.

Table 1 shows the weight percentage and average particle size calculated from XRD data, volume averaged TEM data, and number averaged TEM data. The lower weight percentage sample had an average particle size too small to resolve with XRD. The average diameters calculated from XRD and number averaged TEM data agree well; therefore, the smallest average diameter was taken to be 1.8 nm. Platinum black (Fischer Scientific) and carbon black (Vulcan XC-72) were also included in the study. The average diameter for platinum black (111), (200), and (220) surfaces was determined to be 9.8 nm using Jade 8.0 Software (Material Data, Inc.) to interpret XRD data.

Table 1 Average diameters calculated from crystallographic techniques.

Pt content	d_{xrd}	d_v	d_n
w/w%	*nm*	*nm*	*nm*
30	-	2.8	1.8
50	2.6	3.7	2.6
60	2.9	3.8	2.7
70	3.2	4.3	3.4

Instruments and analytical methods

Approximately 5 – 10 mm of each sample was packed into 0.0435" OD polyimide capillaries (Cole-Parmer EW-95820-09) and sealed at both ends with epoxy. The 11-ID-B beam line at Argonne National Lab was employed to obtain the images of the samples. The beam size was 0.4 mm by 0.4 mm with energy equal to 58.26 keV and wavelength of 0.2128 Å. A liquid nitrogen tank was used to control sample temperature.

Samples were scanned at 80 K and 500 K for 20 min. Samples were then scanned from 80 K to 500 K at a rate of 84 K/hr. Each beam line image was integrated using Fit-2D Software to obtain energy vs Q space. These data were Fourier-sine transformed to generate PDF files, G(r) vs r.

Ex-situ analysis

The inset graph in Figure 6 shows a representative PDF for 50 w/w% Pt/C at T = 81.7 K. The full PDF is truncated around the first peak and shows the experimental data, fitted Gaussian curve, and the difference. The peak position represents the nearest neighbor distance.

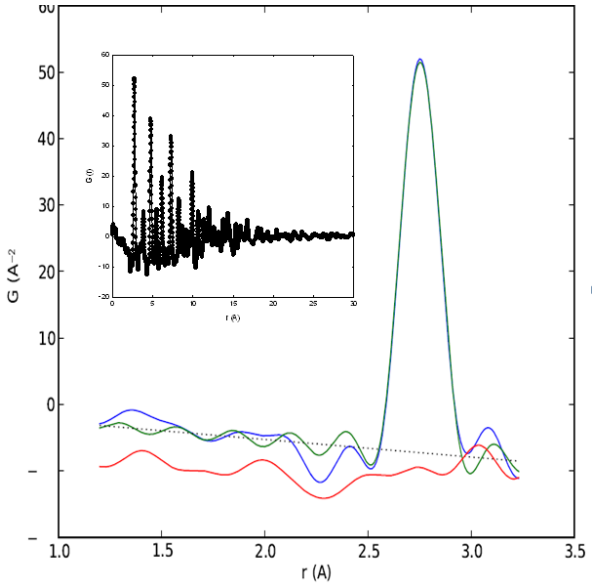

Figure 6 Representative PDF truncated between 1.2 and 3.2 Å to show first Pt-Pt nearest neighbor. Sample was 50 w/w% Pt/C at T = 81.7 K. [- measured PDF, - fitted Gaussian, - difference] Inset shows full PDF.

As mentioned earlier, temperature scans were performed from approximately 80 to 500 K. The following figure shows the peak width of the first Pt-Pt peak versus temperature for all platinum containing samples.

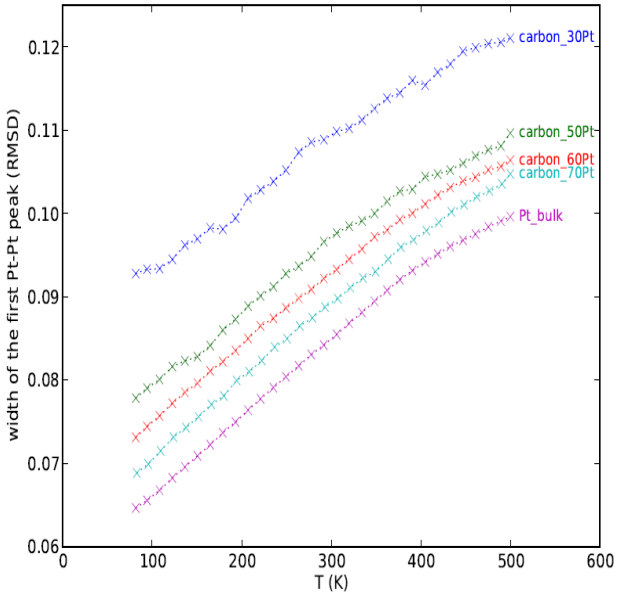

Figure 7 Temperature dependence of Pt-Pt peak width, where width is the variance of the Gaussian function fit to the experimental data.

Unlike crystallographic methods, the peak width corresponds to the variance of the fit Gaussian function, instead of the full width at half maximum familiar to crystallographic studies, and is indicative of bond length variations within a particle. As expected, peak width increases as temperature increases due to thermal vibrations. Additionally, smaller nanoparticles are expected to have larger peak widths since the strain stored in the bond between two surface atoms increases as particles become smaller.[36] Thus, there is a greater variation in bond lengths between surface atoms and internal atoms within the particle. It is also possible that wider particle size distribution in samples contribute to larger peak widths; however, the exact effect is

unknown. The data show that platinum nanoparticles in the size regime of ~2 – 10 nm behave as expected.

Average bond strain (Δa/a) was calculated by the method outlined in [12], where

$$\frac{\Delta a}{a} = \frac{r_{nano} - r_{bulk}}{r_{bulk}} \tag{6}$$

The nearest neighbor distance is denoted by *r*, and the subscript indicates which sample. The value for r_{bulk} was taken from the *Handbook of Inorganic Compounds* as 0.39231 nm.[40] The following figure shows the measured average bond strain as a function of particle diameter and the theoretical value according to Huang et al.[26]

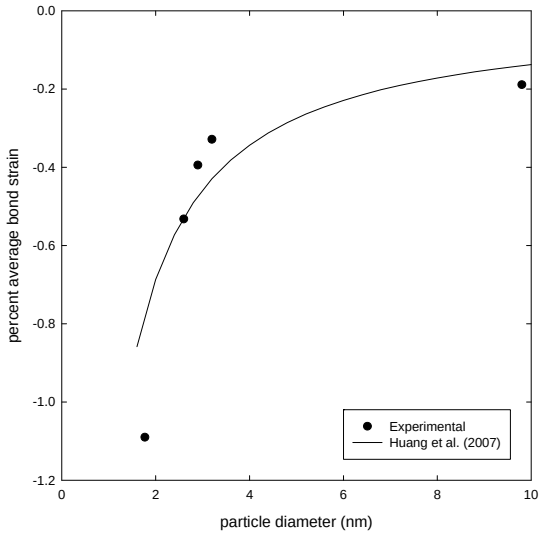

Figure 8 Average bond strain as a function of particle size data displayed from experimental and theoretical results.

The model used to fit the experimental data is based on the notion that surface tension will elastically deform the metal nanoparticle. A nanoparticle is 'taken' from the bulk system. Once removed surface tension will act to compress the particle to a new equilibrium.[26] Forces acting on the spherical nanoparticle are assumed to be symmetric. The stress acting at the interface on the nanoparticle surface in the radial direction is governed by the Young-Laplace equation. Applying these conditions, the percent bond strain is represented by the following equation.[26]

$$\frac{\Delta a}{a} = -\frac{4\sigma}{3\kappa} \cdot \frac{1}{d} \times 100 \tag{7}$$

Percent bond strain and particle diameter are the same as previously defined, and the surface energy, σ, and bulk modulus, κ, are respectively equal to 2.37E-18 J/nm^2 [21] and 2.3E-16 J/nm^3.[41] Application of the model to nanoparticles is questionable as the model assumes a periodic structure, but it has successfully been used to describe bond strain for various metal nanoparticles.[26] Overall, a good fit is obtained with some error that may be explained by the large size distribution present in the samples.

The repeatability of the PDF measurements was studied by observing the first peak position with respect to temperature for all experiments. The following graphs compare the smallest Pt/C samples to the largest.

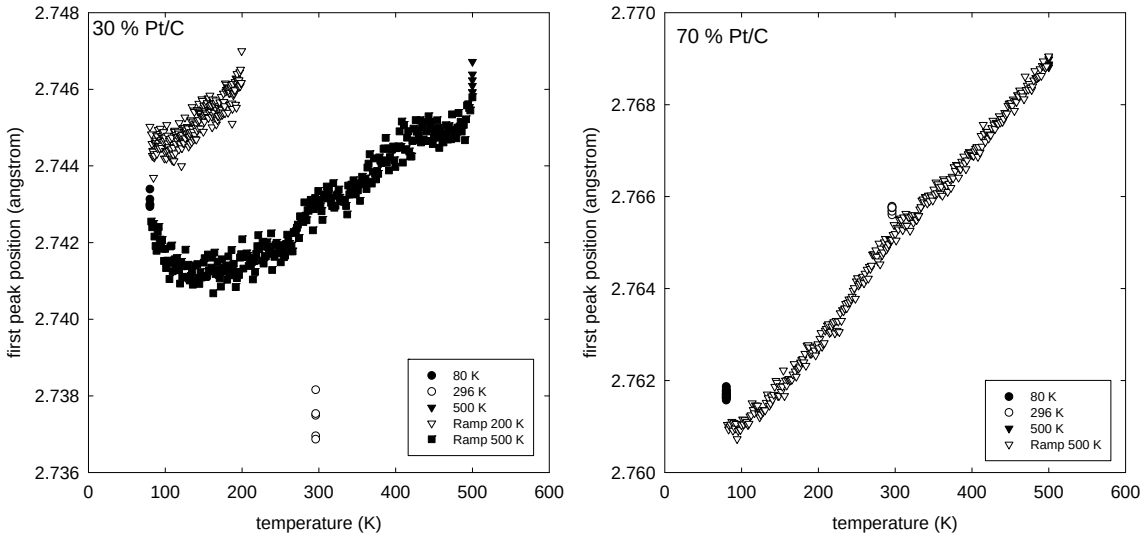

Figure 9 Repeatability data for 30 % Pt/C (left) and 70% Pt/C (right).

The smaller the platinum nanoparticles, the more noise present in PDF measurements. This observation can be explained by the amount of carbon in each sample. The smaller sized sample has a larger percentage of carbon, and the graphite structure file for PDF is incomplete; therefore, a greater graphite presence results in a worse PDF. To resolve this issue, it will be crucial to apply the differential PDF method to smaller sized platinum samples. Additionally, the bond length is higher for the 200 K ramp experiment of 30 % Pt/C. The difference may indicate the sample changes with time. As a comparison, larger platinum particles result in more repeatable data. No trend was seen between first peak position and scan order for any of constant temperature experiments.

Proposed future work

Essential to developing successful and durable alternative energy devices is a fundamental understanding of the conditions that exist throughout the lifetime of a fuel cell and which conditions drive platinum instability. Techniques and results from the following experiments can be applied to other studies contributing to degradation mitigation.

It has been shown that the upper potential is critical to controlling platinum stability.[25] Additionally, post-mortem studies of the catalyst layer and ionomer have been extensively examined after potential cycling experiments.[9, 19] Ferreira and coworkers investigated ECA loss over 10,000 potential cycles.[19] Gravimetric in-situ techniques have been applied to determine oxide species present[42, 43] at high potentials, but to this researcher's knowledge limited in-situ data exists describing catalyst morphology over the lifetime of a PEMFC.[44]

Successful implementation of the PDF technique in platinum stability studies was discussed in the **Experimental** section for powder samples. We plan to use the PDF technique to study the surface changes on the catalyst layer of an MEA throughout several thousand potential cycles.

Four MEAs will be fabricated from each of the TKK samples, to limit variables introduced in this experiment. The MEAs will have a platinum loading of 0.1 mg_{Pt}/cm^2 and 1 mg_{Pt}/cm^2 at the anode and cathode, respectively. Any changes in the PDF can then be attributed to the cathode catalyst later, since the diffracted x-ray intensity will be stronger. Standard electrochemical

techniques, such as cyclic voltammetry and potential cycling will be applied to determine performance of the cell, electrochemically active area, and oxide coverage. Half of the samples will be subjected to ex-situ characterization methods, such as TEM and XRD. Before and after potential cycling experiments the samples will undergo standard crystallographic characterization techniques to show platinum band formation in the membrane, platinum loss from the electrode, and catalyst shape changes.

The PDFs of the remaining samples will be measured in collaboration with Professor Simon Billinge's group, including a commercial MEA as a control sample. Dr. Peter Chupas of Argonne National Lab is helping us develop the experimental set-up. The MEA will be placed in custom fuel cell hardware, shown below.

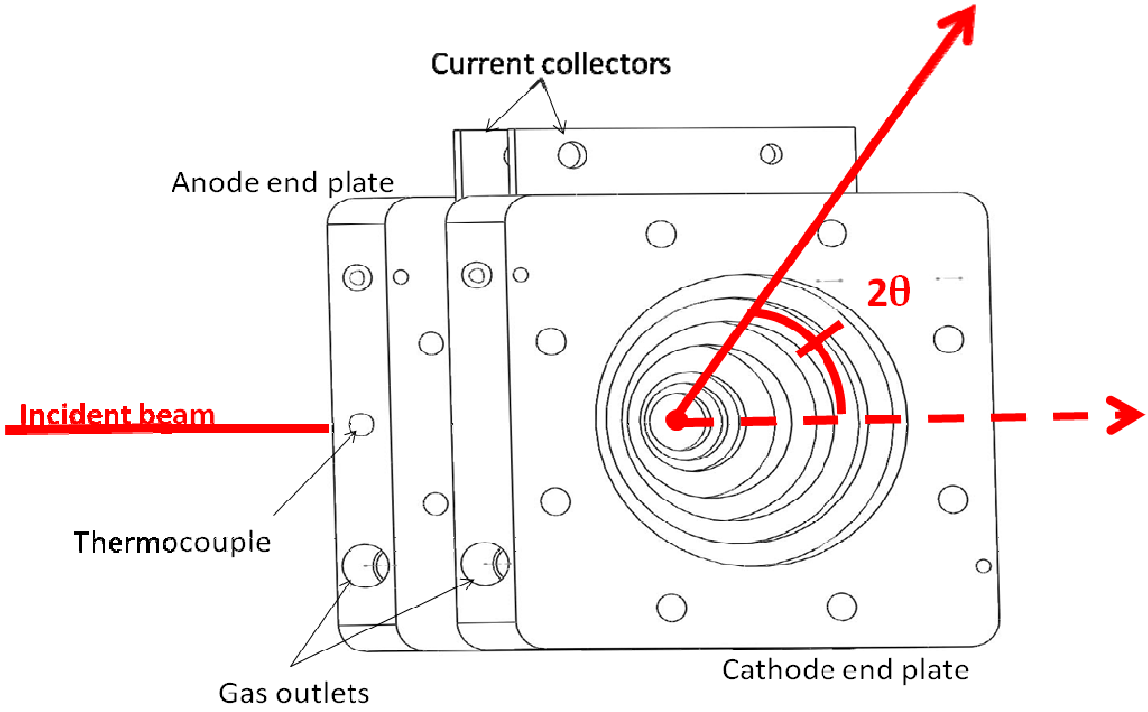

Figure 10 Custom fuel cell hardware with concentric windows at the cathode side for PDF measurements.

The setup allows the full range of 2θ (0˚ to 60˚) to be collected by the image plate detector. The anode side has a small hole, allowing the incident x-ray beam to pass through. The concentric windows at the cathode side allow the diffracted beams to reach the detector with minimal interference. Particle size as a function of time will be extracted from the PDF data. Several thousand potential cycles will be applied so that particle morphology can be studied over the lifetime of a PEMFC. Figure 10 is representative of the data we seek: the PDF as a function of time. Instead of temperature we will be showing the data as a function of potential cycles.

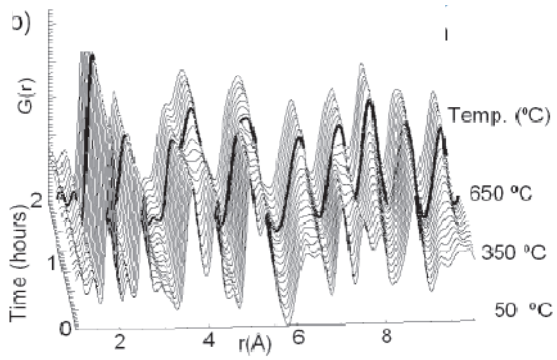

Figure 11 Example PDF of output data.[45]

We hope to complete these experiments by summer 2011. Experiments to be completed further in the future include subnanometer studies. Dr. Stefan Vajda of Argonne National Labs has developed a method for producing monodisperse, size-selected metal nanoparticles.[46] We plan to repeat PDF experiments monitoring G(r) as a function of temperature and potential cycles. Extending the size regime of our data will provide a more complete and fundamental picture of platinum stability.

References

1. Collier, A., et al., *Degradation of polymer electrolyte membranes.* International Journal of Hydrogen Energy, 2006. **31**(13): p. 1838-1854.
2. Curtin, D.E., et al., *Advanced materials for improved PEMFC performance and life.* Journal of Power Sources, 2004. **131**(1-2): p. 41-48.
3. Chen, C. and T.F. Fuller, *The effect of humidity on the degradation of Nafion (R) membrane.* Polymer Degradation and Stability, 2009. **94**(9): p. 1436-1447.
4. Trogadas, P., J. Parrondo, and V. Ramani, *Degradation mitigation in polymer electrolyte membranes using cerium oxide as a regenerative free-radical scavenger.* Electrochemical and Solid State Letters, 2008. **11**(7): p. B113-B116.
5. Gallagher, K., R.M. Darling, and T.F. Fuller, *Carbon-support corrosion mechanisms and models*, in *Handbook of Fuel Cells – Fundamentals, Technology and Applications*, W. Vielstich, H. Yokokawa, and H.A. Gasteiger, Editors. 2009, John Wiley & Sons: West Sussex, United Kingdom. p. 819 - 828.
6. Yu, P.T., et al., *Carbon-support requirements for highly durable fuel cell operation*, in *Polymer Electrolyte Fuel Cell Durability*. 2009, Spring: New York, NY. p. 29 - 53.
7. Jerkiewicz, G., et al., *Surface-oxide growth at platinum electrodes in aqueous H2SO4 Reexamination of its mechanism through combined cyclic-voltammetry, electrochemical quartz-crystal nanobalance, and Auger electron spectroscopy measurements.* Electrochimica Acta, 2004. **49**(9-10): p. 1451-1459.
8. Pourbaix, M., *Atlas of Electrochemical Equilibria in Aqueous Solutions*. 2 ed. 1974, Houston, TX: National Association of Corrosion Engineers.
9. Bi, W., G.E. Gray, and T.F. Fuller, *PEM fuel cell Pt/C dissolution and deposition in nafion electrolyte.* Electrochemical and Solid State Letters, 2007. **10**(5): p. B101-B104.
10. Holby, E.F., et al., *Pt nanoparticle stability in PEM fuel cells: influence of particle size distribution and crossover hydrogen.* Energy & Environmental Science, 2009. **2**(8): p. 865-871.
11. Peng, Z.M. and H. Yang, *Designer platinum nanoparticles: Control of shape, composition in alloy, nanostructure and electrocatalytic property.* Nano Today, 2009. **4**(2): p. 143-164.
12. Masadeh, A.S., et al., *Quantitative size-dependent structure and strain determination of CdSe nanoparticles using atomic pair distribution function analysis.* Physical Review B, 2007. **76**(11): p. 115413-1 - 115413-11.
13. Billinge, S.J.L. and M.G. Kanatzidis, *Beyond crystallography: the study of disorder, nanocrystallinity and crystallographically challenged materials with pair distribution functions.* Chemical Communications, 2004(7): p. 749-760.
14. Aragane, J., T. Murahashi, and T. Odaka, *Change of Pt Distribution in the Active Components of Phosphoric-Acid Fuel-Cell.* Journal of the Electrochemical Society, 1988. **135**(4): p. 844-850.
15. Kinoshita.K, Lundquist.JT, and Stonehart.P, *Potential Cycling Effects on Platinum Electrocatalyst Surfaces.* Journal of Electroanalytical Chemistry, 1973. **48**(2): p. 157-166.
16. Bett, J.A.S., K. Kinoshita, and P. Stonehart, *Crystallite Growth of Platinum Dispersed on Graphitized Carbon-Black .2. Effect of Liquid Environment.* Journal of Catalysis, 1976. **41**(1): p. 124-133.

17. Ross, P.N., *Deactivation and Poisoning of Fuel Cell Catalysts*, in *Catalyst Deactivation*, E.E. Petersen and A.T. Bell, Editors. 1987, Marcel Dekker, Inc. : New York. p. 165 - 187.
18. Shao-Horn, Y., et al., *Instability of supported platinum nanoparticles in low-temperature fuel cells.* Topics in Catalysis, 2007. **46**(3-4): p. 285-305.
19. Ferreira, P.J., et al., *Instability of Pt/C electrocatalysts in proton exchange membrane fuel cells - A mechanistic investigation.* Journal of the Electrochemical Society, 2005. **152**(11): p. A2256-A2271.
20. Ascarelli, P., V. Contini, and R. Giorgi, *Formation process of nanocrystalline materials from x-ray diffraction profile analysis: Application to platinum catalysts.* Journal of Applied Physics, 2002. **91**(7): p. 4556-4561.
21. Darling, R.M. and J.P. Meyers, *Kinetic model of platinum dissolution in PEMFCs.* Journal of the Electrochemical Society, 2003. **150**(11): p. A1523-A1527.
22. Darling, R.M. and J.P. Meyers, *Mathematical model of platinum movement in PEM fuel cells.* Journal of the Electrochemical Society, 2005. **152**(1): p. A242-A247.
23. Bindra, P., S.J. Clouser, and E. Yeager, *Platinum Dissolution in Concentrated Phosphoric-Acid.* Journal of the Electrochemical Society, 1979. **126**(9): p. 1631-1632.
24. Bi, W. and T.F. Fuller, *Modeling of PEM fuel cell Pt/C catalyst degradation.* Journal of Power Sources, 2008. **178**(1): p. 188-196.
25. Chandrasekaran, R., W. Bi, and T.F. Fuller, *Robust design of battery/fuel cell hybrid systems-methodology for surrogate models of Pt stability and mitigation through system controls.* Journal of Power Sources, 2008. **182**(2): p. 546-557.
26. Huang, Z.X., P. Thomson, and S.L. Di, *Lattice contractions of a nanoparticle due to the surface tension: A model of elasticity.* Journal of Physics and Chemistry of Solids, 2007. **68**(4): p. 530-535.
27. Akbarzadeh, H., H. Abroshan, and G.A. Parsafar, *Surface free energy of platinum nanoparticles at zero pressure: A molecular dynamic study.* Solid State Communications, 2010. **150**(5-6): p. 254-257.
28. Fischer-Cripps, A.C., *Introduction to Contact Mechanics*. 2 ed. 2007, New York: Springer.
29. Sun, C.Q., *Size dependence of nanostructures: Impact of bond order deficiency.* Progress in Solid State Chemistry, 2007. **35**(1): p. 1-159.
30. Wang, L.L. and D.D. Johnson, *Shear instabilities in metallic nanoparticles: Hydrogen-stabilized structure of Pt-37 on carbon.* Journal of the American Chemical Society, 2007. **129**(12): p. 3658-3664.
31. Tolman, R.C., *The Effect of Droplet Size on Surface Tension.* Journal of Chemical Physics, 1949. **17**(3): p. 333-337.
32. Arevalo, M.C., et al., *Adsorption, oxidation and reduction of crotyl alcohol on platinum - A DEMS and in situ FTIRS study.* Electrochimica Acta, 2006. **51**(25): p. 5365-5375.
33. Bruchez, M., et al., *Semiconductor nanocrystals as fluorescent biological labels.* Science, 1998. **281**(5385): p. 2013-2016.
34. Tran, P.T., et al., *Use of luminescent CdSe-ZnS nanocrystal bioconjugates in quantum dot-based nanosensors.* Physica Status Solidi B-Basic Research, 2002. **229**(1): p. 427-432.
35. Vermaak, J.S., C.W. Mays, and Kuhlmann.D, *On Surface Stress and Surface Tension .I. Theoretical Considerations.* Surface Science, 1968. **12**(2): p. 128-&.

36. Proffen, T., et al., *Structural analysis of complex materials using the atomic PDF - A practical guide.* Z. Kristallogr., 2003. **218**: p. 132 - 143.
37. Egami, T. and S.J.L. Billinge, *Underneath the Bragg peaks: Structural analysis of complex materials*. 2003, Oxford England: Pergamon Press Elsevier.
38. Petkov, V., et al., *Structure of nanocrystalline materials using atomic pair distribution function analysis: Study of LiMoS2.* Physical Review B, 2002. **65**(9): p. -.
39. Petkov, V., et al., *Application of atomic pair distribution function analysis to materials with intrinsic disorder. Three-dimensional structure of exfoliated-restacked WS2: Not just a random turbostratic assembly of layers.* Journal of the American Chemical Society, 2000. **122**(47): p. 11571-11576.
40. Perry, D.L. and S.L. Phillips, *Handbook of Inorganic Compounds*. 1995, Boca Raton, FL.: CRC Press LLC.
41. *Technical data for the element Platinum in the Periodic Table*. 2010 [cited 2010 04 April]; Available from: http://www.periodictable.com/Elements/078/data.html.
42. Alsabet, M., M. Grden, and G. Jerkiewicz, *Comprehensive study of the growth of thin oxide layers on Pt electrodes under well-defined temperature, potential, and time conditions.* Journal of Electroanalytical Chemistry, 2006. **589**(1): p. 120-127.
43. Birss, V.I., M. Chang, and J. Segal, *Platinum Oxide Film Formation Reduction - an in-Situ Mass Measurement Study.* Journal of Electroanalytical Chemistry, 1993. **355**(1-2): p. 181-191.
44. Smith, M.C., et al., *In situ small-angle X-ray scattering observation of Pt catalyst particle. growth during potential cycling.* Journal of the American Chemical Society, 2008. **130**(26): p. 8112-+.
45. Chupas, P.J., et al., *Probing local and long-range structure simultaneously: An in situ study of the high-temperature phase transition of alpha-AlF3.* Journal of the American Chemical Society, 2004. **126**(15): p. 4756-4757.
46. Vajda, S., et al., *Subnanometre platinum clusters as highly active and selective catalysts for the oxidative dehydrogenation of propane.* Nature Materials, 2009. **8**(3): p. 213-216.

Modeling

This work aims to address the role of particle size distribution on Pt stability. A theoretical model was built based on modified Butler-Volmer equations, platinum oxide surface coverage and interparticle interactions between platinum oxide particles. Preliminary results demonstrated the change in platinum ions concentration across the electrode and membrane and revealed the effect of potential cycling on the particle size. The model was modified further in order to include 5 different particle sizes for each particle size distribution. The same Pt dissolution mechanism was observed during potential cycling (0.5 - 1 V vs. SHE) for all distributions tested and the effect of distribution "width" on Pt^{2+} concentration was demonstrated. Three driving cycles were simulated showing the effect of potential cycling and idle state (OCV) on Pt^{2+} concentration. Ongoing research is focused on the development of a modified version of the model including a log-normal particle size distribution to provide a precise tool for monitoring the particle size distribution as a function of time.

Introduction

The predominant degradation mechanisms in PEFCs can be divided into 5 categories: **1)** mechanical (pinhole formation); **2)** thermal (temperature effects on membrane properties); **3)** electrochemical (formation of hydrogen peroxide and free radicals that attack the polymer membrane); **4)** oxidation of carbon-supports of the cathode catalyst during fuel cell startup and shutdown (1) and **5)** sintering/dissolution of platinum-based cathode catalysts during long-term fuel cell operation (2).

The first models on Pt oxidation at low temperatures were developed by Mott and Cabrera (3-4) assuming that the transport of ionic defects constituted the rate limiting step as well as the electric field was uniform in the oxide and inversely proportional to oxide thickness. The Mott-Cabrera model on platinum oxidation was adopted by several groups (5-10) although its functionality for oxide film thicknesses lower than 1 nm was questioned (11).

Darling and Meyers (12-13) developed the first detailed numerical model for the Pt area loss induced by voltage cycling including potential-dependent dissolution of Pt, chemical dissolution of Pt oxide, and surface tension driven growth of Pt nanoparticles. The platinum on carbon surface coverage by oxide was calculated by empirical Butler-Volmer equations. The intermediate species (adsorbed hydroxyl groups on Pt, PtO_2H, PtOH) of oxygen reduction reaction (ORR) as well as the water adsorption on catalyst surface was not considered.

Shao-Horn and coworkers (14) constructed a thermodynamic-kinetic model, one dimensional along the direction normal to the cathode. To simulate in-situ experimental conditions it was hypothesized that platinum diffused to the anode, crossover hydrogen was considered in the model and the electrolyte volume and Pt loading were 10^{-4} mL and 0.4 $mgcm^{-2}$ respectively. To simulate ex-situ experimental conditions, it was assumed that there was no hydrogen crossover, Pt diffused from the cathode and Pt was mixed every 200 cycles, while the volume of electrolyte and Pt loading were 130 mL and 0.01 $mgcm^{-2}$ respectively. It was predicted that in the ex-situ experimental environment, Pt surface area loss and particle size distribution was dominated by

coarsening. In the simulated in-situ environment, crossover hydrogen increased the Pt mass flow from the particle surface resulting to an increase of Pt surface area loss. Simulations have demonstrated that Pt stability was improved once the Pt particle size was increased from 2 to 5 nm (in-situ experimental conditions), although the effect of particle size enhancement on electrochemically active surface area or Pt activity was not taken into account.

Pt reduction by crossover hydrogen was taken under consideration in the models developed by Fuller's group (15-17). The deposited Pt forms a band in the ionomer during potential H_2 / O_2 cycling, and a model based on gas (H_2 and O_2) crossover rates was proposed to describe its location (15). The Pt band position calculated theoretically agreed with the experimental band position detected with scanning electron microscopy (SEM) (15). Moreover, the effect of reactant gas partial pressure and RH on Pt dissolution was investigated (16). It was observed that an increase in RH results in higher Pt degradation rates as an approximate three- and two-fold increase to the loss of cathode Pt mass and Pt electrocatalyst surface area (ECA) at 100 %RH (compared to 50 %RH) was observed (16). The effect of reactant gas partial pressure on cathode degradation was found to be insignificant (16). Finally, cathode catalyst degradation was modeled using a bi-modal particle-size distribution (17) refining Darling-Meyers models (12-13). Pt particle growth was revealed through mass exchange of Pt between small and large particles. However, additional Pt degradation processes such as Pt nanoparticles coarsening or Pt cluster formation on carbon support need to be included (17).

Despite these modeling attempts, there is partial information about the role of Pt particle size distribution (18), Pt^{2+} ions diffusivity, and platinum oxide chemical dissolution reaction on catalyst degradation rate. It is still unknown how the uniformity of the particle size distribution affects Pt stability under potential cycling over time. It is expected that the more narrow the distribution, the greater the stability under potential cycling. At the same time, it is difficult and presumably costly to produce uniform particle sizes. What's more the system may be unstable to small variations, and thus the advantages of uniform particle size may be lost quickly during potential cycling. This works seeks to quantify these effects. In the present study, it is hypothesized that Pt nanoparticles follow a narrow size distribution (~ 1.8 to 3.2 nm) and their radii changes are monitored during ~ 600 potential cycles assuming that i) Pt nanoparticles are spherical (radius r); ii) interface reaction controls the particle growth during Ostwald ripening; iii) hydrogen concentration is constant (~ 1M); and iv) interactions between the platinum surface and the electrochemical double layer are neglected.

Pt dissolution model

Pt degradation mechanism is described by three electrochemical reactions, namely Pt electrochemical dissolution (~ 1.2V vs. SHE; reaction 1), Pt oxidation (~ 0.98 V vs. SHE; reaction 2) and Pt precipitation by hydrogen reduction (reaction 3) while platinum oxide chemical dissolution is not considered due to unknown kinetics (13). Modified Butler-Volmer equations (13, 17) are used to describe the reaction rates considering the size dependency of particle stability (Kelvin equation), platinum oxide surface coverage and interparticle interactions between platinum oxide particles.

$$Pt \leftrightarrow Pt^{2+} + 2e^{-} \quad [1]$$

$$r_{1j} = k_{1j}\vartheta_j^{vacant}[\exp(aa_1 n_1 \frac{F(E-U_{1j})}{RT}) - \frac{C_{Pt^{+2}}}{C_{Pt^{+2}_{ref}}}\exp - ac_1 n_1 \frac{F(E-U_{2j})}{RT}) \quad j = \text{small, medium, large}$$

$$\text{Pt} + \text{H}_2\text{O} \leftrightarrow \text{PtO} + 2\text{H}^+ + 2\text{e}^- \qquad [2]$$

$$r_{2j} = k_2[\exp(\frac{-\omega\vartheta_j}{RT})\exp(\frac{aa_2 n_2 F(E-U_{2j})}{RT}) - C_H^2\vartheta_j \exp(\frac{-ac_2 n_2 F(E-U_{2j})}{RT})] \quad j = \text{small, medium, large}$$

$$\text{Pt}^{2+} + \text{H}_2 \leftrightarrow \text{Pt} + 2\text{H}^+, \qquad [3]$$

where the thermodynamic potentials U_{1j} and U_{2j} are given by the following equations [4]

$$U_{1j} = U_1^o - \frac{\sigma_{Pt} MW_{Pt}}{\rho_{Pt} R_j} \quad j = \text{small, medium, large}$$

$$U_{2j} = U_2^o + \frac{1}{2F}(\Delta\mu_{PtO}^o + \frac{\sigma_{PtO} MW_{PtO}}{\rho_{PtO} R_j} - \frac{\sigma_{Pt} MW_{Pt}}{\rho_{Pt} R_j}) \quad j = \text{small, medium, large}$$

A mass balance of Pt ions provides the overall Pt^{2+} concentration [5]

$$\frac{\partial C_{Pt^{2+}}}{\partial t} = D_{Pt^{2+}} \frac{\partial^2 C_{Pt^{2+}}}{\partial x^2} + \frac{A_i}{\varepsilon_c} r_{1j} \quad j = \text{small, medium, large}$$

while surface coverage and radius of Pt particles are given by the following equations [6]

$$\frac{d\partial_j}{dt} = \frac{r_{2j}}{\Gamma_{\max}} + \frac{2\vartheta_j MW_{Pt}}{R_j \rho_{Pt}}(r_{1j} + r_{2j}) \quad j = \text{small, medium, large}$$

$$\frac{dR_j}{dt} = -\frac{MW_{Pt}}{\rho_{Pt}}(r_{1j} + r_{2j}) \quad j = \text{small, medium, large}$$

Volume-average particle radius equations are introduced in the model in order to use different Pt particle size distributions and examine their distribution trend (17). [7]

$$RR_j = \frac{\sum_j N_j R_j^4}{\sum_j N_j R_j^3} \quad j = \text{small, medium, large; x} = \text{distance away from cathode}$$

Finally, the current density is [8]

$$i = 2aFL(r_{1j} + r_{2j})$$

where L the thickness of the catalyst layer.

Results and Discussion

The distribution of Pt concentration in the cathode catalyst layer was determined theoretically by gPROMS®. Model equations were integrated in the software and solved using the backward finite difference equation; Pt^{2+} diffusivity was approximately $1.5 \cdot 10^{-13}$ m^2s^{-1} and Pt dissolution and oxidation reaction constants were $3 \cdot 10^{-6}$ and $7 \cdot 10^{-6}$ $molm^{-2}s^{-1}$ respectively (17). Figure 1 represents Pt^{2+} concentration for three different electrodes containing small (~ 1.8 nm), small and medium (~ 1.8 – 2.7 nm) and small, medium and large Pt particles (~ 1.8 – 3.2 nm). Concentration values are very similar for all different systems tested and slowly reduced near the catalyst/membrane interface due to Pt dissolution at high potentials and migration into membrane (19-20). Energy dispersive x-ray (EDX) mapping of platinum concentration under scanning transmission electron microscopy (STEM) are in progress.

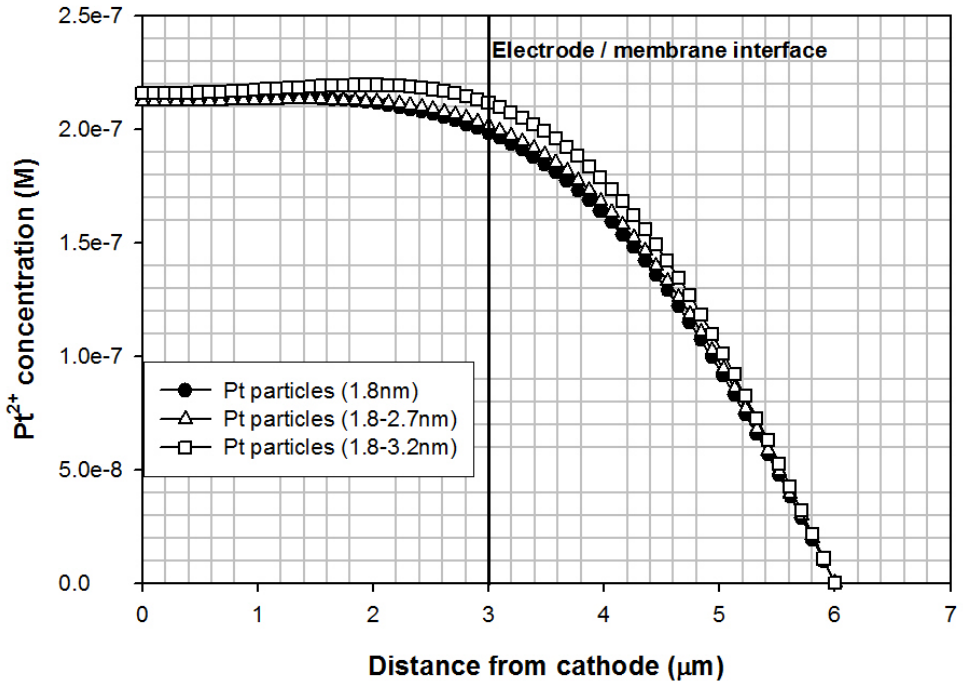

Figure 12. Pt^{2+} concentration profile across the electrode and membrane (Pt^{+2} diffusivity ~ $1.5 \cdot 10^{-13}$ m^2s^{-1}).

Figures 2 and 3 represent the evolution of Pt particle radii in the electrode under potential cycling. The electrocatalyst layer consists of small (intial radius ~ 1.8 nm), medium (initial radius ~ 2.6 nm) and large (initial radius ~ 3.2 nm) nanoparticles and is subjected to potential cycling from 0.5 to 1 V vs standard hydrogen electrode (100 s per cycle, 626 cycles). It is demonstrated that the coarsening of Pt nanoparticles in the electrode proceeds via Ostwald ripening (21-24). Large particle radius is decreasing until Pt^{+2} concentration reaches a pseudo-

steady state (at approximately 400th potential cycle) while after this critical point interparticle transport takes place resulting in the further decrease of small and medium radii particles and the simultaneous enlargement of large particles.

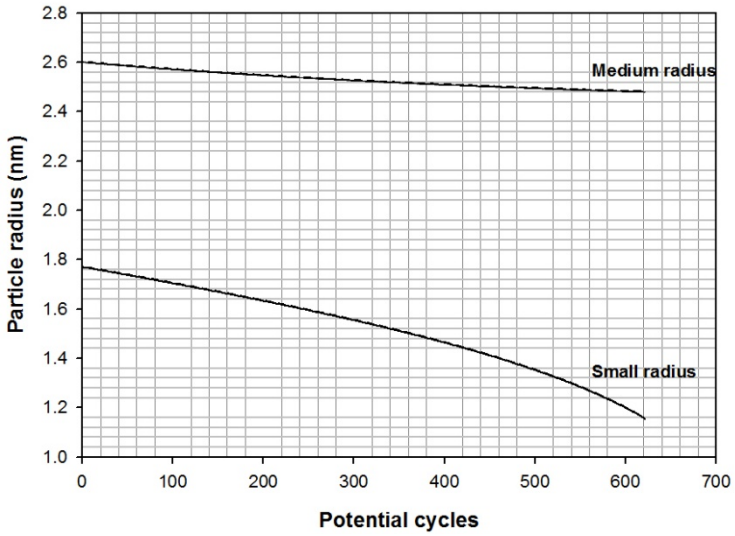

Figure 2. Pt particle size (small and medium) evolution under potential cycling (0.5 - 1 V vs SHE, 100 s/cycle, 626 cycles).

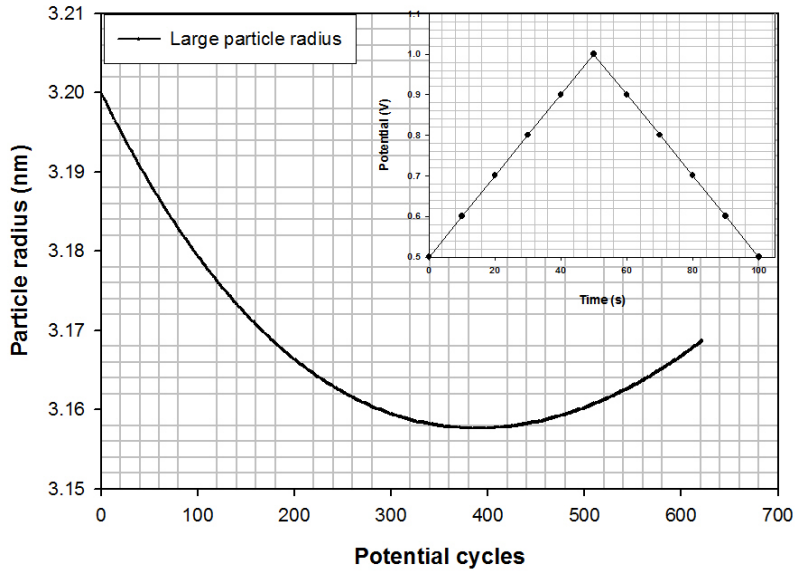

Figure 3. Pt particle size (large) evolution under potential cycling (0.5 - 1 V vs SHE, 100 s/cycle, 626 cycles).

Furthermore, the model was modified in order to include 5 different particle sizes in each particle size distribution. Four different particle size distributions were used (2-4-6-10-15 nm, 3-5-7-9-12 nm, 2-4-6-8-10 nm and 2-5-8-11-14 nm) and the electrode was cycled between 0.5 and 1 V vs. SHE for ~600 cycles (100 sec per cycle). The effect of Ostwald ripening on particle size

can be clearly seen; small and medium radii particles (Fig. 4 & 5) had a ~ 20% and 10% loss of their size at the end of potential cycling respectively. Large particles (Fig. 6 & 7; 6 and 10 nm from the first size distribution, 7 and 9 nm from the 2nd, 6 and 8 nm from the 3rd and 8 and 11 from the 4th) remained constant throughout the potential cycling while extra-large particles were continuously growing till the end of potential cycling (Fig. 8; 15 nm particle size).

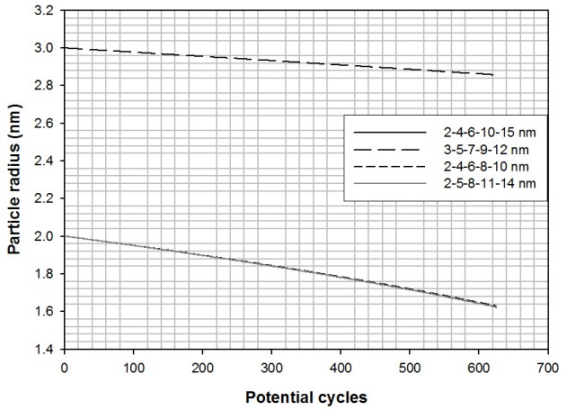

Figure 4: Small particle radii vs. potential cycles (0.5 - 1 V vs. SHE, 100sec/cycle, 5 different particle sizes in each size distribution).

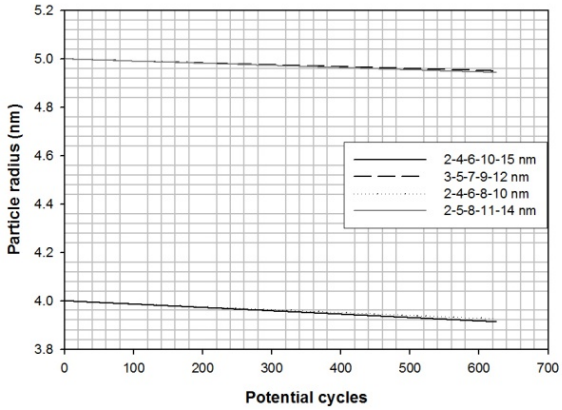

Figure 5: Medium particle radii vs. potential cycles (0.5 - 1 V vs. SHE, 100sec/cycle, 5 different particle sizes in each size distribution).

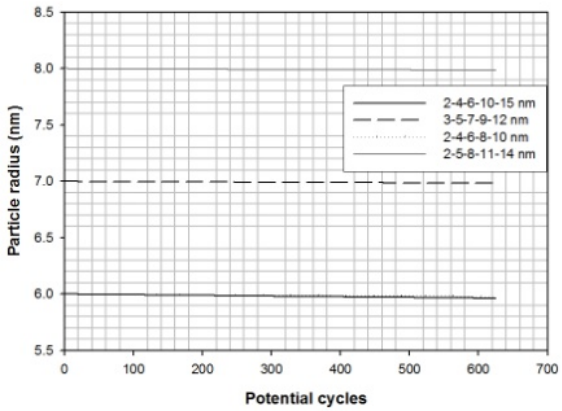

Figure 6: Large particle radii vs. potential cycles (0.5 - 1 V vs. SHE, 100sec/cycle, 5 different particle sizes in each size distribution).

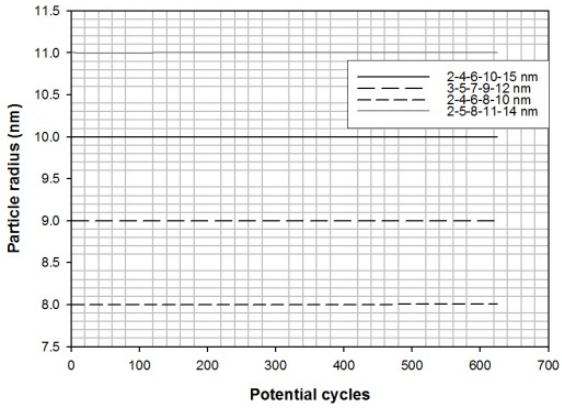

Figure 7: Extra-large particle radii vs. potential cycles (0.5 - 1 V vs. SHE, 100sec/cycle, 5 different particle sizes in each size distribution).

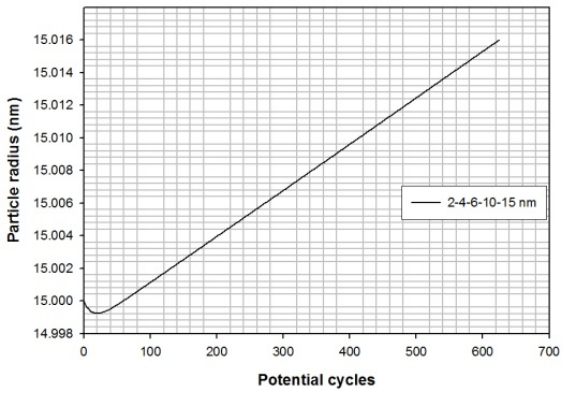

Figure 8: Largest particle radius vs. potential cycles (0.5 - 1 V vs. SHE, 100sec/cycle, 2-4-6-10-15 nm distribution).

Pt^{2+} concentration vs. potential cycles graph (Fig. 9) demonstrated that the "width" of size distribution affects Pt^{2+} concentration; the narrower the size distribution, the higher the Pt^{2+} concentration.

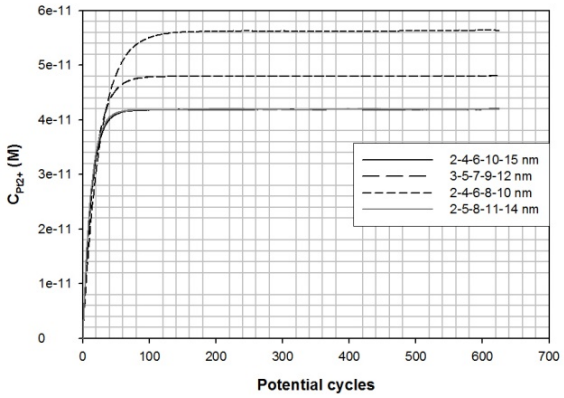

Figure 9: Pt^{2+} concentration (M) vs. potential cycles (0.5 - 1 V vs. SHE, 100sec/cycle, 2-4-6-10-15 nm distribution).

In addition, three driving cycles were simulated: **1)** 2 h potential cycling (0.5 - 1 V vs. SHE) - 3 h at OCV (~ 0.9 V vs. SHE) - 2 h potential cycling (0.5-1 V vs. SHE), **2)** 1 h potential cycling - 1 h at OCV - 1 h potential cycling and **3)** 3 h potential cycling - 10 h at OCV - 1 h potential cycling. Fig. 10-12 represent Pt^{2+} concentration vs. time of the 2-4-6-8-10 nm size distribution. Two conclusions can be derived from these graphs: **i)** Pt^{2+} concentration does not reach a steady state for potential cycling less than 2 h; and **ii)** the longer the vehicle remains at idle state (OCV) the higher the Pt^{2+} concentration in the electrode. Similar trends were observed in the other size distributions tested.

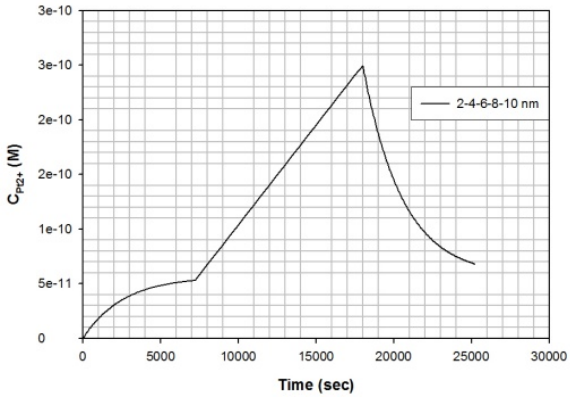

Figure 10: Pt^{2+} concentration (M) vs. time (sec). (driving cycle 1; 2-4-6-8-10 nm distribution).

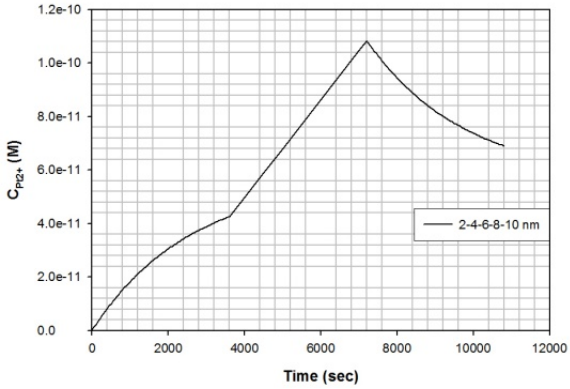

Figure 11: Pt^{2+} concentration (M) vs. time (sec). (driving cycle 2; 2-4-6-8-10 nm distribution).

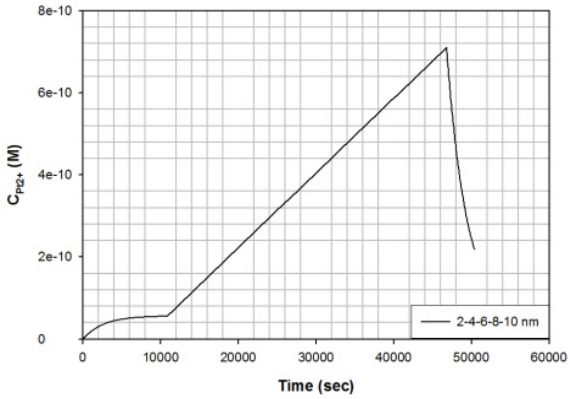

Figure 12: Pt^{2+} concentration (M) vs. time (sec). (driving cycle 3; 2-4-6-8-10 nm distribution).

Modified Pt dissolution model

Currently, programming code is modified to contain a population balance (25) that better describes the particle size distribution. Pt degradation mechanism is described by two electrochemical reactions, namely Pt electrochemical dissolution (~ 1.2V vs. SHE; reaction 1) and Pt oxidation (~ 0.98 V vs. SHE; reaction 2), while modified Butler-Volmer equations (13, 17) are used to describe the reaction rates considering the size dependency of particle stability (Kelvin equation), platinum oxide surface coverage and interparticle interactions between platinum oxide particles.

$$Pt \leftrightarrow Pt^{2+} + 2e^- \qquad [1]$$

$$r_1 = k_1 \theta^{vacant} [\exp(aa_1 n_1 \frac{F(E-U_1)}{R_B T}) - \frac{C_{Pt^{+2}}}{C_{Pt^{+2}_{ref}}} \exp - ac_1 n_1 \frac{F(E-U_1)}{RT})$$

$$Pt + H_2O \leftrightarrow PtO + 2H^+ + 2e^- \qquad [2]$$

$$r_2 = k_2[\exp(\frac{-\omega\theta}{R_B T})\exp(\frac{aa_2 n_2 F(E-U_2)}{R_B T}) - C_H^2\theta\exp(\frac{-ac_2 n_2 F(E-U_2)}{R_B T})]$$

Thermodynamic potentials U_1 and U_2 are given by the following equations

$$U_1 = U_1^o - \frac{1}{2F}\frac{\sigma_{Pt} MW_{Pt}}{\rho_{Pt} R} \quad [3]$$

$$U_2 = U_2^o + \frac{1}{2F}(\Delta\mu_{PtO}^o + \frac{\sigma_{PtO} MW_{PtO}}{\rho_{PtO} R} - \frac{\sigma_{Pt} MW_{Pt}}{\rho_{Pt} R}) \quad [4]$$

A mass balance of Pt ions provides the overall Pt^{2+} concentration

$$\frac{\partial C_{Pt^{+2}}}{\partial t} = D_{Pt^{+2}}\frac{\partial^2 C_{Pt^{+2}}}{\partial x^2} + \int_0^{number} \mathrm{f}\cdot \mathrm{r}_1 \cdot \frac{N}{V}\cdot 8\pi R dR \quad [5]$$

while surface coverage is given by the following equations

$$\frac{d\theta}{dt} = \frac{r_2}{\Gamma_{\max}} + \frac{2\theta MW_{Pt}}{R\rho_{Pt}}(r_2) \quad [6]$$

$$\theta + \theta^{vac} = 1 \quad [7]$$

Finally, the population balance equation is incorporated into the model

$$-\frac{\partial(\frac{dR}{dt} f)}{\partial R} = \frac{\partial f}{\partial t} \Leftrightarrow \frac{\partial\left(\frac{MW_{Pt}}{\rho_{Pt}}(r_1 + r_2) f\right)}{\partial R} = \frac{\partial f}{\partial t} \quad [8]$$

Where f the log-normal particle size distribution

$$f(R, t=0) = \frac{1}{R\ln(\sigma_g)\sqrt{2\pi}}\exp\left\{\frac{-\left[\ln\left(\frac{R}{R_g}\right)\right]^2}{2(\ln\sigma_g)^2}\right\} \quad [9]$$

The modified Pt dissolution model is under development and will provide a precise tool for monitoring the particle size distribution as a function of time.

Conclusions

A model was built to examine the effect of Pt particle size distribution on Pt stability. Modified Butler-Volmer equations were used to describe Pt dissolution and oxidation while three different Pt particle sizes were included to study their effect on Pt radius under potential cycling and Pt^{+2} concentration across the electrode and membrane. Preliminary results revealed that the governing mechanism of Pt dissolution under potential cycling is Ostwald ripening where large particles grow at the expense of small ones. Further simulations were conducted using 5 different particle sizes for each particle size distribution. The same Pt dissolution mechanism (Ostwald ripening) was observed during potential cycling (0.5 - 1 V vs. SHE) for all distributions tested and the effect of distribution "width" on Pt^{2+} concentration was demonstrated. In addition, three driving cycles were simulated showing that i) Pt^{2+} concentration does not reach a steady state for potential cycling less than 2 h; and ii) the longer the vehicle remains at idle state (OCV) the higher the Pt^{2+} concentration in the electrode. Currently, a modified version of the model is being tested including a population balance that better describes the particle size distribution; it will provide a precise tool for monitoring the particle size distribution as a function of time.

TABLE I. Model variables and constants.

Variables	
a (m^2)	MEA area ($25cm^2 = 2.5e^{-3}m^2$)
A_j (m^2m^{-3})	Specific surface areas of small, medium and large particles
C_H	Relative proton activity (1)
C_{Pt+2} ($molm^{-3}$)	Pt ions concentration
$C_{Pt+2ref}$ ($molm^{-3}$)	Ptions reference concentration (1000 $molm^{-3}$)
D_{Pt+2} (m^2s^{-1})	Pt ions diffusion coefficient
E (V)	Applied potential
F ($Cequiv^{-1}$)	Faraday's constant (96485 $Cequiv^{-1}$)
k_1 ($molm^{-2}s^{-1}$)	Pt dissolution reaction rate constant
k_2 ($molm^{-2}s^{-1}$)	Pt oxidation reaction rate constant
L (m)	Distance between electrode and membrane interface ($6 \cdot 10^{-9}$ m)
MW_{Pt} ($kgmol^{-1}$)	Pt molecular weight (0.1951 $kgmol^{-1}$)
MW_{PtO} ($kgmol^{-1}$)	PtO molecular weight (0.2110 $kgmol^{-1}$)
n_1 ($equivmol^{-1}$)	Equivalent electrons transferred per mole of Pt dissoluted (2 $equivmol^{-1}$)
n_2 ($equivmol^{-1}$)	Equivalent electrons transferred per mole of Pt oxidized (2 $equivmol^{-1}$)
N_j	Pt particles in each cathode mesh
R (m)	Particle radius
R_B ($Jmol^{-1}K^{-1}$)	Universal gas constant (8.314 $Jmol^{-1}K^{-1}$)
R_g	Geometric mean radius
RR_j (m)	Volume average Pt particles in cathode
r_1	Reaction rate for Pt dissolution ($molm^{-2}s^{-1}$)
r_2	Reaction rate for Pt oxidation ($molm^{-2}s^{-1}$)
Scanrate ($Vsec^{-1}$)	0.01 $Vsec^{-1}$
T (K)	Temperature (~ 298 K)
t (sec)	Time
U_1	Thermodynamic Pt dissolution potential (V)

U_2	Thermodynamic Pt oxidation potential (V)
U^o_1 (V)	Thermodynamic potential of Pt dissolution (~ 1.2 V vs SHE)
U^o_2 (V)	Thermodynamic potential of Pt oxidation (~ 0.98 V vs SHE)
V	Volume
aa_1, ac_1	Anodic and cathodic transfer coefficient of Pt dissolution
aa_2, ac_2	Anodic and cathodic transfer coefficient of Pt oxidation
ε_c, ε_M	Ionomer volume fraction in the cathode and membrane
Γ_{max} ($molm^{-2}$)	Maximum oxide at Pt surface ($2.18e^{-5}$ $molm^{-2}$)
$\Delta\mu_{Pt}^o$ ($Jmol^{-1}$)	Fitted chemical potential shift for PtO
θ_j	Total surface oxide coverage of small, medium and large Pt particles
θ_j^{vacant}	Pt oxide vacancy at the top surface monolayer of small, medium and large Pt particles
ρ_{Pt} (kgm^{-3})	Pt metal density (21,090 kgm^{-3})
ρ_{PtO} (kgm^{-3})	PtO metal density (14,100 kgm^{-3})
σ_g	Geometric standard deviation
σ_{Pt} (Jm^{-2})	Surface tension of Pt nanoparticles (2.37 Jm^{-2})
σ_{PtO} (Jm^{-2})	Surface tension of PtO nanoparticles (1 Jm^{-2})
ω ($Jmol^{-1}$)	PtO-PtO interaction coefficient

References

1. C. A. Reiser, L. Bregoli, T. W. Patterson, J. S. Yi, J. D. Yang, M. L. Perry, and T. D. Jarvi, *Electrochem. Solid-State Lett.*, **8**, A273 (2005).
2. H. A. Gasteiger, W. Gu, B. Litteer, R. Makharia, B. Brady, M. Budinski, E. Thompson, F. T. Wagner, S. G. Yan, and P. T. Yu, in *Mini-Micro Fuel Cells*, S. Kakac, A. Pramuanjaroenkij and L. Vasiliev, Editors, p. 225, Springer Netherlands (2008).
3. N. F. Mott, *Trans. Faraday Soc.*, **35**, 1175 (1939).
4. N. Cabrera, and N. F. Mott, *Rep. Prog. Phys.*, **12**, 163 (1948-1949).
5. J. L. Ord, and F. C. Ho, *J. Electrochem. Soc.*, **118**, 46 (1971).
6. A. Damjanovic, L. S. R. Yeh, and J. F. Wolf, *J. Electrochem. Soc.*, **127**, 1945 (1980).
7. A. Damjanovic, L. S. R. Yeh, and J. F. Wolf, *J. Electrochem. Soc.*, **127**, 1951 (1980).
8. A. Damjanovic, L. S. R. Yeh, and J. F. Wolf, *J. Electrochem. Soc.*, **126**, 555 (1979).
9. A. Damjanovic, A. T. Ward, B. Ulrick, and M. O'Jea, *J. Electrochem. Soc.*, **122**, 471 (1975).
10. L. B. Harris, and A. Damjanovic, *J. Electrochem. Soc.*, **122**, 593 (1975).
11. R. Ghez, *J. Chem. Physics*, **58**, 1838 (1973).
12. J. P. Meyers, and R. M. Darling, *J. Electrochem. Soc.*, **153**, A1432 (2006).
13. R. M. Darling, and J. P. Meyers, *J. Electrochem. Soc.*, **150**, A1523 (2003).
14. E. F. Holby, W. Sheng, Y. Shao-Horn, and D. Morgan, *Energy & Environmental Science*, **2**, 865 (2009).
15. W. Bi, G. E. Gray, and T. F. Fuller, *Electrochem. Solid-State Lett.*, **10**, B101 (2007).
16. W. Bi, Q. Suna, Y. Deng, and T. F. Fuller, *Electrochim. Acta*, **54**, 1826 (2009).
17. W. Bi, and T. F. Fuller, *J. Power Sources*, **178**, 188 (2008).
18. K. Kinoshita, J. T. Lundquist, and P. Stonehart, *Electroanal. Chem. Interfac. Electrochem.*, **48**, 157 (1973).
19. J. Li, P. He, K. Wang, M. Davis, and S. Ye, *ECS Trans.*, **3**, 743 (2006).

20. J. Li, in *PEM Fuel Cell Electrocatalysts and Catalyst Layers*, J. Zhang, Editor, p. 1075, Springer-Verlag, London (2008).
21. I. M. Lifshitz, and V. V. Slyozov, *J. Phys. Chem. Solids*, **19**, 35 (1965).
22. C. G. Granqvist, and R. A. Buhrman, *J. Catal.*, **42**, 477 (1976).
23. P. J. Ferreira, G. J. la O', Y. Shao-Horn, D. Morgan, R. Makharia, S. Kocha, and H. A. Gasteiger, *J. Electrochem. Soc.*, **152**, A2256 (2005).
24. Y. Shao-Horn, W. C. Sheng, S. Chen, P. J. Ferreira, E. F. Holby, and D. Morgan, *Top. Catal.*, **46**, 285 (2007).
24. 25. S.E LeBlanc, and H.S. Fogler, *AIChE J*, **33**, 54 (1987).
1.